Stability of dynamic coherent states in intrinsic Josephson-junction stacks near internal cavity resonance

A. E. Koshelev
Materials Science Division, Argonne National Laboratory, Argonne, Illinois 60439, USA
(Received 25 August 2010; published 16 November 2010)

Stacks of intrinsic Josephson junctions in the resistive state can by efficiently synchronized by the internal cavity mode resonantly excited by the Josephson oscillations. We study the stability of dynamic coherent states near the resonance with respect to small perturbations. Three states are considered: the homogeneous and alternating-kink states in zero magnetic field and the homogeneous state in the magnetic field near the value corresponding to half flux quantum per junction. We found two possible instabilities related to the short-scale and long-scale perturbations. The homogeneous state in modulated junction is typically unstable with respect to the *short-scale alternating phase deformations* unless the Josephson current is completely suppressed in one half of the stack. The kink state is stable with respect to such deformations and homogeneous state in the magnetic field is only stable within a certain range of frequencies and fields. Stability with respect to *the long-range deformations* is controlled by resonance excitations of fast modes at finite wave vectors and typically leads to unstable range of the wave vectors. This range shrinks with approaching the resonance and increasing the in-plane dissipation. As a consequence, in finite-height stacks the stability frequency range near the resonance increases with decreasing the height.

DOI: 10.1103/PhysRevB.82.174512 PACS number(s): 74.50.+r, 85.25.Cp, 74.81.Fa

I. INTRODUCTION

Superconducting tunneling junctions are natural voltage-tunable sources of electromagnetic radiation due to the ac Josephson effect.[1] As radiation from a single junction is very small, large-size arrays of artificially fabricated junctions have been used to enhance power of electromagnetic radiation, see early reviews[2,3] and more recent papers.[4,5] The main challenge is to synchronize all junctions in the array. In this case the total emitted power is expected to be proportional to the square of the total number of junctions.

Intrinsic Josephson junctions in the high-temperature layered superconducting materials,[6] such as $Bi_2Sr_2CaCu_2O_8$ (BSCCO), provide a very promising base for developing coherent generators of electromagnetic radiation which may operate in the terahertz frequency range. These materials have several important advantages in comparison with artificial structures made out of conventional superconductors including (i) the large packing density of the junctions, (ii) a large value of the superconducting gap (up to 60 mev) which allows to bring the Josephson frequency into the terahertz range, and (iii) possibility to make very large arrays of practically identical junctions.

The stack of junctions can be a powerful, coherent, and efficient generator only if the oscillations of the superconducting phases in all junctions are synchronized. Due to weak intrinsic interaction between the junctions, this is a challenging task. One possible way to synchronization is to use interactions between the junctions via the generated external radiation.[7] In this case, for efficient coupling to the radiation field, a junction stack (mesa) must have small lateral size (<10 μm) and contain a very large number of junctions ($>10^4$). Such a mesa would be a frequency-tunable source with the considerable power-conversion efficiency. The obvious technological challenge of this design is the requirement to fabricate structures with such large number of almost identical junctions. This design has not yet been implemented in practice.

A very promising route to efficient synchronization is to excite an internal cavity resonance in finite-size samples (mesas).[8,9] Being excited, the resonance mode can entrain oscillations in a very large number of junctions. The frequency of this mode is set by the lateral size of the mesa and for the resonance frequency in the terahertz range the width has to be rather large (40–100 μm). The experimental demonstration[8] and confirmation[10,11] of this mechanism marks a major advance in the quest for Josephson terahertz generators.

In general, the structure of the coherent state and the mechanism of pumping energy into the cavity mode are nontrivial issues. Homogeneous phase oscillations at zero magnetic field do not couple to the Fiske modes. Such coupling can be facilitated by introducing an external modulation of the Josephson critical current density.[9] In this case the amplitudes of the generated standing wave and of the produced radiation are proportional to the strength of the modulation.

An interesting alternative possibility has been demonstrated recently.[12–14] It was found that near the resonance an inhomogeneous synchronized state is formed. In this state, the stack spontaneously splits into two subsystems with different phase-oscillation patterns, corresponding to the alternating phase kinks and antikinks *statically* located near the center. This leads to a static phase shift between the oscillations in the two subsystems varying from 0 to 2π in a narrow region near the stack center. In spite of this c-axis inhomogeneity, the oscillating electric and magnetic fields are almost homogeneous in all the junctions. The formation of this state promotes efficient pumping of the energy into the cavity resonance.

Another potential candidate for the coherent state producing strong emission is a homogeneous state in the external magnetic field, also known as a rectangular Josephson-vortex

 ©2010 The American Physical Society

lattice. In spite of strong experimental efforts, the existence of this state has not yet been clearly demonstrated, except for small-size stacks at very small velocity.[15] It was argued that in the large-size crystals the rectangular lattice is almost always unstable.[16] For a finite-size system the stability analysis of the homogeneous state has been performed recently[17] and stability regions have been found.

As large-size stacks have a huge number of degrees of freedom, stability of the coherent states with respect to small perturbations is an important and nontrivial issue. Linear stability analysis amounts to calculating the full frequency spectrum for small perturbations with respect to steady-state coherent solutions and verifying that there are no exponentially growing perturbations. The stability analysis allows to evaluate the range of parameters where the coherent states are possible. For linear arrays of point junctions the stability analysis has been performed in Refs. 18 and 19. In this case stability is strongly influenced by the external load. A large array of the small-size intrinsic Josephson junctions can be stabilized by the radiation field which acts similar to the external capacitive load.[7]

In this paper we perform a systematic comparative analysis of the linear stability of different coherent states in the array of extended Josephson junctions near the resonance. We revealed two types of instabilities. The *short-wavelength* instability corresponding to the alternating phase deformations develops for states which have regions of negative local time-averaged Josephson coupling. This instability is sensitive to the nature of the dynamic state. The homogeneous state in the modulated junctions is typically prone to this kind of instability. The *long-wavelength* instability with wavelengths larger than the London penetration depth λ appears due to the parametric resonance excitation of the fast modes at finite wave vectors. Analysis of this instability is essentially identical for all dynamic states. The instability criterion depends on several factors including behavior of the resonance frequency shift with increasing the in-plane and c-axis wave vectors and the relation between damping of the uniform mode and modes at finite wave vectors. The most essential parameters influencing stability include the shift of the Josephson frequency with respect to the resonance, the stack height, and the in-plane quasiparticle dissipation. The paper is organized as follows. In Sec. II we present the dynamic phase equations and coherent solutions near the internal resonance. In Sec. III we derive the linear dynamic equations for small perturbations with respect to steady states. In Sec. IV we consider the short-wavelength instabilities of different steady states and present the numerical test for these instabilities in the stacks with modulated critical current. In Sec. V we describe the stability analysis with respect to the long-wave deformations and numerical verification of this analysis. The description of numerical simulations used to check some of our analytical results is presented in Appendix.

II. PHASE DYNAMIC EQUATIONS AND COHERENT SOLUTIONS

The dynamic equations for the Josephson-junction stacks have been derived in several papers[20] and have been used in different forms in numerous simulation and theoretical studies.[21] These equations can be written in the reduced form as coupled equations for the phases φ_n and dimensionless magnetic fields $\mathbf{h}_n=(h_{x,n},h_{y,n})$,

$$\frac{\partial^2\varphi_n}{\partial\tau^2}+(1-\alpha\nabla_n^2)\left[\nu_c\frac{\partial\varphi_n}{\partial\tau}+g(x)\sin\varphi_n-e_{ijz}\partial_i h_{j,n}\right]=0, \tag{1}$$

$$\ell^2\nabla_n^2 h_{j,n}-\left(1+\nu_{ab}\frac{\partial}{\partial\tau}\right)[h_{j,n}-e_{ijz}\partial_i\varphi_n]=0. \tag{2}$$

Here $i,j=x,y$, e_{ijz} is the Levi-Civita symbol ($e_{xyz}=-e_{yxz}=1$). The units in these equations are selected as follows: $1/\omega_p$ is the unit of time with ω_p being the plasma frequency, the c-axis London penetration depth λ_c is the unit of length, $\Phi_0/(2\pi\lambda_c s)$ is the unit of the magnetic field. The function $g(x)$ describes possible modulation of the Josephson current which was suggested as the way to couple to the internal resonance.[9] We consider both modulated and unmodulated $[g(x)=1]$ cases. The equations depend on four parameters, the layer-charging parameter α,[22] two damping parameters, $\nu_c=4\pi\sigma_c/(\varepsilon_c\omega_p)$, $\nu_{ab}=4\pi\sigma_{ab}/(\varepsilon_c\gamma^2\omega_p)$, and the ratio $\ell=\lambda/s$, where σ_c and σ_{ab} are the components of quasiparticle conductivity, λ is the in-plane London penetration depth, and γ is the anisotropy factor. We will study a finite-size stack (mesa) containing N junctions with lateral sizes L_x and L_y. We consider the case $L_y\gg L_x$.

We tested some of our analytical results with numerical simulations. The numerical procedure is the same as in Ref. 13. For completeness, details of the numerical simulations are described in Appendix.

A. Coherent states in zero magnetic field

We consider the stack in the coherent resistive state, in which all junctions have identical voltage drops. In this state the dynamical phase can be written as[23]

$$\varphi_n(x,\tau)\approx\omega\tau+\theta_n(x,\tau).$$

Further, we assume that the Josephson frequency ω is close to the in-phase resonance frequency $\omega_m=m\pi/L_x$ and the resonance cavity mode is excited inside the mesa meaning that the oscillating phase has the large resonance contribution $\theta_n(x,\tau)\sim\cos(m\pi x/L_x)\cos(\omega\tau+\alpha)$. We will mostly focus on the experimentally relevant case of the fundamental mode $m=1$. One can distinguish two particular cases: for a homogeneous (uniform) solution the phases $\theta_n(x,\tau)$ are identical in all junctions and for an inhomogeneous (nonuniform) solution the phases $\theta_n(x,\tau)$ vary from junction to junction. For the homogeneous solution,[9] $\theta_n(x,\tau)=\theta(x,\tau)$, Eqs. (1) and (2) reduce to the sine-Gordon equation,

$$\frac{\partial^2\varphi}{\partial\tau^2}+\nu_c\frac{\partial\varphi}{\partial\tau}+g(x)\sin\varphi-\frac{\partial^2\varphi(x,\tau)}{\partial x^2}=0. \tag{3}$$

In this case coupling to the resonance mode is only induced by the external modulation $g(x)$. Representing the oscillating phase as $\theta(x,\tau)=\mathrm{Re}[\theta_\omega(x)\exp(-i\omega\tau)]$, we obtain an equation for the complex amplitude $\theta_\omega(x)$,

$$(\omega^2 + i\nu_c\omega)\theta_\omega + \frac{\partial^2\theta_\omega}{\partial x^2} = ig(x). \tag{4}$$

This equation has to be supplemented by the boundary conditions accounting for radiation. For symmetric mesas general boundary conditions can be presented in the following form:

$$\frac{\partial\theta_\omega}{\partial x}(L_x) = i\zeta\theta_\omega(L_x) + i\tilde{\zeta}\theta_\omega(0), \tag{5a}$$

$$\frac{\partial\theta_\omega}{\partial x}(0) = -i\zeta\theta_\omega(0) - i\tilde{\zeta}\theta_\omega(L_x). \tag{5b}$$

The coefficients ζ and $\tilde{\zeta}$ depend on the particular geometry. For example, for the case of an isolated mesa on a metallic plate with thin metallic contact on the top

$$\zeta \approx \frac{\omega^2 L_z}{2\varepsilon_c}\left[1 - \frac{2i}{\pi}\ln\left(\frac{C}{k_\omega L_z}\right)\right],$$

$$\tilde{\zeta} \approx -\frac{\omega^2 L_z}{2\varepsilon_c}[J_0(k_\omega L_x) + iN_0(k_\omega L_x)],$$

where $k_\omega = \omega/c$, $L_z = Ns$ is the stack height, $J_0(z)$ and $N_0(z)$ are the Bessel functions, and $C \sim 1$. As ζ and $\tilde{\zeta}$ are small, near the resonance we can look for solution in the form

$$\theta_\omega = \psi\cos(m\pi x/L_x) + \upsilon(x),$$

where $\upsilon(x)$ is the small correction accounting for the radiation boundary conditions. With this ansatz, Eq. (4) becomes

$$(\omega^2 - \omega_m^2 + i\nu_c\omega)\psi\cos(m\pi x/L_x) + (\omega^2 + i\nu_c\omega)\upsilon + \frac{\partial^2\upsilon}{\partial x^2} = ig(x).$$

As υ is small, we can approximately replace $(\omega^2 + i\nu_c\omega)\upsilon \to \omega_m^2\upsilon$ and look for correction satisfying the mode-matching condition $\omega_m^2\upsilon + \partial^2\upsilon/\partial x^2 \propto \cos(m\pi x/L_x)$. In this case, $\upsilon(x)$ can be found as

$$\upsilon(x) \approx a\psi(x - L_x/2)\sin(m\pi x/L_x)$$

giving $\omega_m^2\upsilon + \partial^2\upsilon/\partial x^2 = 2a\psi\cos(m\pi x/L_x)(m\pi/L_x)$. Substituting this result into the previous equation and taking projection to the mode, we obtain

$$\psi = \frac{ig_m}{\omega^2 - \omega_m^2 + 2a(m\pi/L_x) + i\nu_c\omega},$$

where $g_m = (2/L_x)\int_0^{L_x}\cos(m\pi x/L_x)g(x)dx$ is the coupling parameter. The complex constant a has to be found from the boundary conditions Eq. (4) where in the right-hand side we can neglect $\upsilon(x)$. In this case the approximate boundary conditions for the correction become

$$\frac{\partial\upsilon}{\partial x}(L_x) \approx i[(-1)^m\zeta + \tilde{\zeta}]\psi,$$

$$\frac{\partial\upsilon}{\partial x}(0) \approx -i[\zeta + (-1)^m\tilde{\zeta}]\psi$$

and they give identical results for a,

$$a \approx (2i/m\pi)[\zeta + (-1)^m\tilde{\zeta}].$$

The amplitude of the cavity mode can finally be represented as

$$\psi = \frac{ig_m}{(1+\alpha_r)\omega^2 - \omega_m^2 + i(\nu_r + \nu_c)\omega}, \tag{6}$$

where

$$\nu_r = \frac{4}{\omega L_x}\mathrm{Re}[\zeta + (-1)^m\tilde{\zeta}] = \frac{2\omega L_z}{\varepsilon_c L_x}[1 - (-1)^m J_0(k_\omega L_x)]$$

determines radiation contribution to the damping[9,24] and

$$\alpha_r = -\frac{4}{L\omega^2}\mathrm{Im}[\zeta + (-1)^m\tilde{\zeta}] \approx \frac{L_z}{\pi\varepsilon_c L_x}\left[\ln\left(\frac{C}{k_\omega L_z}\right) + (-1)^m\frac{\pi}{2}N_0(k_\omega L_x)\right]$$

determines the resonance frequency shift due to radiation. This small frequency shift is frequently neglected. However, it will be essential for the long-range stability analysis. Therefore, the homogeneous oscillating phase near the resonance can be represented as

$$\theta(x,\tau) \approx -\mathrm{Im}\left[\frac{g_m\exp(-i\omega\tau)}{(1+\alpha_r)\omega^2 - \omega_m^2 + i\nu\omega}\right]\cos\left(\frac{m\pi x}{L_x}\right), \tag{7}$$

where $\nu = \nu_c + \nu_r$ is the total mode-damping parameter.[9]

The homogeneous solution is not the only possible coherent state. A spectacular example of an inhomogeneous coherent solution is the alternating-kink state recently reported in Refs. 12 and 13. For this state the phase distribution is given by

$$\theta_n(x,\tau) = (-1)^n\theta_k(x) + \theta(x,\tau),$$

where, for the fundamental mode, the static-kink phase $\theta_k(x)$ changes from 0 to π near the center. As the region of this change is extremely narrow,[13] in the equation for the homogeneous oscillating phase $\theta(x,\tau)$ one can approximate $\theta_k(x)$ with the step function $\theta_k(x) \to \pi\Theta(x - L_x/2)$, where $\Theta(x) = 0$ for $x < 0$ and $\Theta(x) = 1$ for $x > 0$. Within this approximation, such a state becomes equivalent to the stack with modulated current density with the modulation function $g_k(x) = \mathrm{sgn}(x - L_x/2)$. In this case the homogeneous part of the oscillating phase is again given by Eq. (7), where for $m = 1$, $g_m \to g_{k,1} \approx 4/\pi$. While for the homogeneous solution coupling to the resonance mode only exists due to the external modulation, for the alternating-kink state such coupling is self-generated.

B. Homogeneous solution in magnetic field

We also consider the homogeneous resonance solution induced by the external magnetic field h_e applied along y direction,

$$\varphi(x,\tau) = \omega\tau + h_e x + \theta(x,\tau)$$

in a stack without the external modulation, $g(x)=1$. The oscillating phase $\theta(x,\tau)=\mathrm{Re}[\theta_\omega(x)\exp(-i\omega\tau)]$ is determined by the following equation:

$$(\omega^2 + i\nu_c\omega)\theta_\omega + \frac{\partial^2\theta_\omega}{\partial x^2} = i\exp(-ih_e x).$$

We will mainly focus on the most interesting case of the fundamental mode and magnetic fields corresponding to a magnetic flux through each junction close to half-flux quantum, $h_e=\pi/L_x$, providing the most efficient coupling to this resonance. The homogeneous solution for the junction stack is essentially identical to the corresponding solution for a single junction,[25] see also Refs. 17 and 26. In particular, when the frequency is close to the resonance frequency ω_m, the dominating contribution to the oscillating phase again has the resonance form given by Eq. (7) with

$$g_m \to g_{h,m} = \frac{2}{L_x}\int_0^{L_x} dx\,\cos(m\pi x/L_x)\exp(-ih_e x)$$
$$= -\frac{2i[1-(-1)^m\exp(-ih_eL_x)]h_eL_x}{(h_eL)^2-(m\pi)^2} \qquad (8)$$

being the coupling parameter due to the magnetic field. In contrast to the zero-field case, this parameter is a complex number. For the fundamental mode

$$g_{h,1} = \frac{4ih_eL_x\exp[-ih_eL_x/2]\cos[h_eL_x/2]}{\pi^2 - h_e^2L_x^2}. \qquad (9)$$

In particular, $g_{h,1}=1$ for $h_eL_x=\pi$. This function is shown in the upper left plot of Fig. 1.

III. EQUATIONS FOR SMALL PERTURBATIONS WITH RESPECT TO COHERENT DYNAMIC STATE

We will study the linear stability of the homogeneous solution with respect to small perturbations. A similar analysis has been done in a recent paper[17] for the homogeneous solution in magnetic field. We found, however, several important instabilities which were missed in this paper.

We consider first the case of the homogeneous state in modulated junctions. With very good accuracy this analysis can also be applied to the kink state because c-axis inhomogeneities in this state are located in a very narrow region near the center. Perturbing the homogeneous solution, $\varphi_n(x,\tau)=\omega\tau+\theta(x,\tau)+\vartheta_n(\mathbf{r},\tau)$ and $\mathbf{h}_n(\mathbf{r},\tau)=\mathbf{h}_n^{(0)}(x,\tau)+\tilde{\mathbf{h}}_n(\mathbf{r},\tau)$, we obtain the linear equations for small perturbations $\vartheta_n(\mathbf{r},\tau)$ and $\tilde{\mathbf{h}}_n(\mathbf{r},\tau)$,

$$\frac{\partial^2\vartheta_n}{\partial\tau^2} + (1-\alpha\nabla_n^2)\times\left[\nu_c\frac{\partial\vartheta_n}{\partial\tau} + g(x)C(x,\tau)\vartheta_n - e_{ijz}\partial_i\tilde{h}_{j,n}\right] = 0, \qquad (10)$$

$$\ell^2\nabla_n^2\tilde{h}_{j,n} - \left(1+\nu_{ab}\frac{\partial}{\partial\tau}\right)[\tilde{h}_{j,n} - e_{ijz}\partial_i\vartheta_n] = 0, \qquad (11)$$

where $C(x,\tau)\equiv\cos[\omega\tau+\theta(x,\tau)]$. Due to this oscillating cosine, perturbations are not monochromatic, oscillations with the frequency Ω are coupled with the frequencies $\Omega\pm\omega$. At $\omega\gg 1$ we can look for solution in the form

$$\vartheta_n(\mathbf{r},\tau) \approx \sum_{q,k_y}\cos[q(n+1/2)]\cos(k_y y)\exp(-i\Omega\tau) \times \sum_{\beta=0,\pm1}\tilde{\vartheta}_{\mathbf{k},\beta}(x)\exp(i\beta\omega\tau)$$

with

$$q = \pi m_z/(N+1), \quad k_y = \pi m_y/L_y \qquad (12)$$

and neglect other frequency components. For simple treatment of the c-axis modes, we assumed that the stack is bounded by metallic contacts which can be approximated by ideal conductors.[24] In this presentation $\Omega\equiv\Omega(k_y,q)$ is the complex eigenfrequency which has to be found from Eqs. (10) and (11) and the boundary conditions. The state is stable only if $\mathrm{Im}[\Omega(k_y,q)]<0$ for all k_y and for all q's from 0 to π. Separating the slow and fast parts in Eqs. (10) and (11), using relation

$$g(x)C(x,\tau)\vartheta_n(\mathbf{r},\tau) \approx \frac{g(x)}{2}\sum_{q,k_y}\cos[q(n+1/2)]\cos(k_y y) \times\left[\tilde{\vartheta}_{\mathbf{k},0}\sum_{\beta=\pm1}\exp(i\beta\omega\tau - i\Omega\tau) + \sum_{\beta=\pm1}\tilde{\vartheta}_{\mathbf{k},\beta}\exp(-i\Omega\tau)\right],$$

and, excluding the magnetic fields,

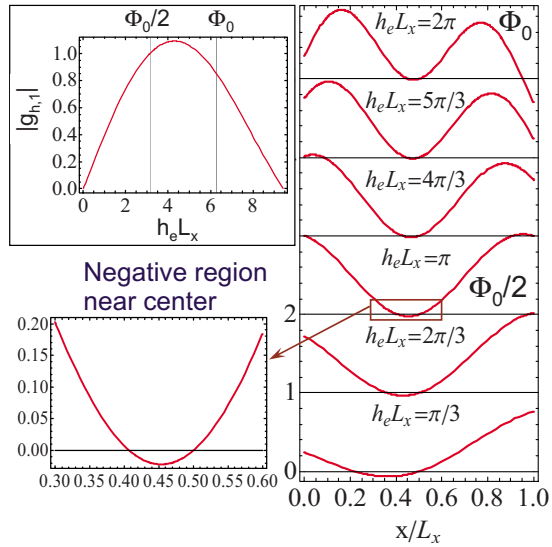

FIG. 1. (Color online) Upper left plot shows the field dependence of the coupling parameter $|g_{h,1}|$, Eq. (9). Right plot illustrates shapes of the local averaged Josephson coupling $U(x)/U_\omega$, Eq. (21), for different magnetic fields and for $\nu\omega/(\omega_1^2-\omega^2)=0.3$. Lower left plot shows blowup of the region near the center for $h_eL_x=\pi$ to illustrate existence of the region with $U(x)<0$ which may lead to the short-scale instability.

$$\tilde{h}_{i,\mathbf{k},\beta} = \frac{1}{1+\ell^2\tilde{q}^2/[1-i\nu_{ab}(\Omega-\beta\omega)]} e_{ijz}\partial_j\tilde{\vartheta}_{\mathbf{k},\beta}$$

with $\beta=0,\pm 1$ and $\tilde{q}=2\sin(q/2)$, we obtain coupled equations for the slow and fast phase oscillations, see also Refs. 7, 16, and 17,

$$(\tilde{\Omega}_0^2 - g(x)\bar{C} - G_{q,0}^{-2}k_y^2)\tilde{\vartheta}_{\mathbf{k},0} + G_{q,0}^{-2}\frac{\partial^2\tilde{\vartheta}_{\mathbf{k},0}}{\partial x^2} = \frac{g(x)}{2}\sum_{\beta=\pm 1}\tilde{\vartheta}_{\mathbf{k},\beta}, \tag{13}$$

$$(\tilde{\Omega}_\beta^2 - G_{q,\beta}^{-2}k_y^2)\tilde{\vartheta}_{\mathbf{k},\beta} + G_{q,\beta}^{-2}\frac{\partial^2\tilde{\vartheta}_{\mathbf{k},\beta}}{\partial x^2} = \frac{g(x)\tilde{\vartheta}_{\mathbf{k},0}}{2}, \tag{14}$$

where we introduced notations

$$\tilde{\Omega}_\beta^2 \equiv (\Omega-\beta\omega)^2/(1+\alpha\tilde{q}^2) + i\nu_c(\Omega-\beta\omega),$$

$$G_{q,\beta}^2 \equiv 1 + \ell^2\tilde{q}^2/[1-i(\Omega-\beta\omega)\nu_{ab}].$$

Using $\varphi=\omega\tau+\mathrm{Re}[\theta_\omega(x)\exp(-i\omega\tau)]$, the time-averaged cosine $\bar{C}(x)\equiv\langle\cos\varphi\rangle_\tau$ can be evaluated as

$$\bar{C}(x) \approx -\mathrm{Im}[\theta_\omega(x)]/2 \approx -\frac{g_m[(1+\alpha_r)\omega^2-\omega_m^2]}{[(1+\alpha_r)\omega^2-\omega_m^2]^2+\nu^2\omega^2}\frac{\cos(m\pi x/L_x)}{2}. \tag{15}$$

Equations (13) and (14) have to be supplemented with the boundary conditions. At finite q, coupling to the external fields is negligible and with high accuracy we can use simple nonradiative boundary conditions

$$\frac{\partial\tilde{\vartheta}_{\mathbf{k},\beta}}{\partial x} = 0 \quad \text{for } x=0,L_x. \tag{16}$$

The stability analysis reduces to computing spectrum of complex eigenfrequencies $\Omega(\mathbf{k})$ from Eqs. (13) and (14) with nonradiative boundary conditions and finding out if there are regions in k space where $\mathrm{Im}[\Omega(\mathbf{k})]>0$.

Case of homogenous state in external magnetic field

The above derivation can be directly extended to the case of the homogeneous state in external magnetic field. Perturbing the homogeneous solution, $\varphi_n(x,\tau)=\omega\tau+h_ex+\theta(x,\tau)+\vartheta_n(\mathbf{r},\tau)$, we obtain Eqs. (10) and (11) for small perturbation $\vartheta_n(x,\tau)$, where now we have $g(x)=1$ and $C(x,\tau)\equiv\cos[\omega\tau+h_ex+\theta(x,\tau)]$. Separating again the slow and fast components in the oscillating phase Eq. (12), and using

$$C(x,\tau)\vartheta_n(x,\tau) \approx \frac{1}{2}\sum_q \cos[q(n+1/2)]\exp(-i\Omega\tau) \times \sum_{\beta=\pm 1}[\tilde{\vartheta}_{\mathbf{k},0}\exp[i\beta(\omega\tau+h_ex)] + \tilde{\vartheta}_{\mathbf{k},\beta}\exp(-i\beta h_ex)],$$

we obtain coupled equations for the slow and fast phase oscillations, which are identical to Eqs. (13) and (14) with replacements

$$\frac{g(x)}{2}\sum_{\beta=\pm 1}\tilde{\vartheta}_{\mathbf{k},\beta} \to \frac{1}{2}\sum_{\beta=\pm 1}\tilde{\vartheta}_{\mathbf{k},\beta}\exp(-i\beta h_ex),$$

$$\frac{g(x)\tilde{\vartheta}_{\mathbf{k},0}}{2} \to \frac{\tilde{\vartheta}_{\mathbf{k},0}}{2}\exp[i\beta h_ex]$$

in the right-hand sides of these equations. The average in time cosine $\bar{C}(x)\equiv\langle\cos\varphi\rangle_\tau$ can be evaluated as

$$\bar{C}(x) = -\mathrm{Re}\left[\frac{g_{h,m}\exp[ih_ex]}{(1+\alpha_r)\omega^2-\omega_m^2+i\nu\omega}\right]\frac{\cos(m\pi x/L_x)}{2}.$$

In the following sections we will analyze different instabilities of the dynamic coherent states.

IV. SHORT-WAVELENGTH INSTABILITY

A. Modulated junction

Consider first the region $\ell\tilde{q}\gg 1$. In this case instability develops only for the homogeneous in the y-direction perturbations, $k_y=0$, and we only consider such perturbations. In this regime the derivative term in the fast part Eq. (14) becomes small and can be neglected giving the estimate

$$\tilde{\vartheta}_{\mathbf{k},\beta} \approx \frac{g(x)}{2}\left[\frac{(\Omega-\beta\omega)^2}{1+\alpha\tilde{q}^2} + i\nu_c(\Omega-\beta\omega)\right]^{-1}\tilde{\vartheta}_{\mathbf{k},0},$$

meaning that, roughly, $\tilde{\vartheta}_{\mathbf{k},\beta}\sim\tilde{\vartheta}_{\mathbf{k},0}/\omega^2\ll\tilde{\vartheta}_{\mathbf{k},0}$. Substituting this estimate into the Eq. (13) for the slow part, we conclude that coupling to the fast terms in this regime is weak and can be neglected. Therefore, the equation for the slow part becomes

$$[\tilde{\Omega}^2 - U(x)]\tilde{\vartheta}_{\mathbf{k},0} + G_{q,0}^{-2}\frac{\partial^2\tilde{\vartheta}_{\mathbf{k},0}}{\partial x^2} = 0, \tag{17}$$

where $U(x)=g(x)\bar{C}(x)$ determines the local plasma frequency. For the lowest mode we obtain

$$U(x) = \frac{g(x)g_1[\omega_1^2-(1+\alpha_r)\omega^2]/2}{[\omega_1^2-(1+\alpha_r)\omega^2]^2+\nu^2\omega^2}\cos(\pi x/L_x). \tag{18}$$

For large q we can use the simple boundary condition $\partial\tilde{\vartheta}_{\mathbf{k},0}/\partial x=0$ at the edges, $x=0,L_x$. As the local "spring constant" $U(x)$ determines the local plasmon frequency $\Omega_{\mathrm{loc}}\propto\pm\sqrt{U(x)}$, the existence of regions with negative $U(x)$ is a potential source of instability. This instability may be eliminated by the gradient term which we have to verify. Consider for definiteness the lowest mode and *negative* coupling parameter, $g_1<0$. The simplest modulation giving such coupling is monotonically increasing $g(x)$. In this case at $\omega<\omega_1$ the spring constant $U(x)$ is negative at $x<L_x/2$ and has minimum near the edge $x=0$ where $g(x)$ is the smallest. Therefore, the region for potential instability is located near the left edge, at $x\ll L_x$. As the most unstable mode is localized near $x=0$, we can expand $U(x)$ with respect to x

$$g(x)\cos(\pi x/L_x) \approx g(0)\left[1 + a_1 x - \frac{a_2}{2}x^2\right]$$

with

$$a_1 = g'(0)/g(0), \quad a_2 = (\pi/L_x)^2 - g''(0)/g(0)$$

giving the equation

$$\left[\tilde{\Omega}^2 + U_\omega\left(1 + a_1 x - \frac{a_2}{2}x^2\right)\right]\tilde{\vartheta}_{\mathbf{k},0} + G_q^{-2}\frac{\partial^2 \tilde{\vartheta}_{\mathbf{k},0}}{\partial x^2} = 0$$

with

$$U_\omega \equiv \frac{g(0)|g_1|[\omega_1^2 - (1+\alpha_r)\omega^2]/2}{[\omega_1^2 - (1+\alpha_r)\omega^2]^2 + \nu^2\omega^2} > 0.$$

From this equation we estimate,

$$\tilde{\Omega}^2 \approx -U_\omega\left[1 + \frac{a_1^2}{2a_2} - C\sqrt{\frac{a_2}{U_\omega G_q^2}}\right]$$

with

$$\frac{a_2}{U_\omega G_q^2} = \frac{(\pi/L)^2 - g''(0)/g(0)}{1 + \ell^2\tilde{q}^2/[1 - i\Omega\nu_{ab}]}\frac{[\omega_1^2 - (1+\alpha_r)\omega^2]^2 + \nu^2\omega^2}{g(0)|g_1|[\omega_1^2 - (1+\alpha_r)\omega^2]/2}$$

and $C \sim 1$. Roughly, the system can only be stable if $|a_2 U_\omega G_q^{-2}| \gtrsim 1$ for all q's. As $|G_q^{-2}|$ has minimum at $q = \pi(\tilde{q} = 2)$, it is sufficient to check the stability condition at this value of q. Skipping numerical factors on the order of unity, we can approximately write the stability criterion as

$$\frac{g(0)g_1(\omega_1^2 - \omega^2)}{(\omega_1^2 - \omega^2)^2 + \nu^2\omega^2} < \frac{\pi^2}{4\ell^2 L_x^2}. \tag{19}$$

This condition is very hard to satisfy because the right-hand side of this equation is very small due to $\ell L_x \gg 1$. Therefore, *the homogeneous solution is almost always unstable with respect to alternating deformations localized near the edge with suppressed Josephson coupling*. The formal reason for the large-q instability is that the local spring constant in Eq. (18) changes sign due to the factor $\cos(\pi x/L_x)$. This instability would be completely eliminated if the modulation function $g(x)$ would also changes sign in the middle. It is practically impossible to prepare such modulation artificially. The best artificial modulation for which the homogeneous state is stable with respect to the short-scale perturbations is steplike modulation for which the Josephson current *completely suppressed* in one half of the stack, $g(x)=0$ for $x < L_x/2$. In this case the plasma frequency is zero in this half and stability is achieved due to the gradient term in Eq. (17).

We will demonstrate below that the alternating-kink solution is stable with respect to the large-q perturbation because it generates an effective modulation changing sign in the middle of the stack making the spring constant positive in the whole stack. Another interesting case is the stack in the magnetic field corresponding to half-flux quantum per junction. In this case the linearly growing contribution to the phase changes from 0 to π across the junction which is similar to a sign-changing modulation. We will consider these cases in more detail in the following sections.

B. Absence of short-wavelength instability for the alternating-kink state

The stability analysis for the modulated system can be directly applied to alternating-kink state. It is crucial, however, that the effective modulation function $g_k(x)$ is close to a step function changing from 1 to -1 in the middle of the stack, i.e., it changes sign in the middle which compensates change in sign in the factor $\cos(\pi x/L_x)$. This eliminates the short-scale instability. Indeed, the effective spring constant in Eq. (18), which determines the local oscillation frequency, can be evaluated as

$$U_k(x) = g_k(x)\bar{C}(x) \approx \frac{g_{k,1}[\omega_1^2 - (1+\alpha_r)\omega^2]/2}{[\omega_1^2 - (1+\alpha_r)\omega^2]^2 + \nu^2\omega^2}|\cos(\pi x/L_x)|. \tag{20}$$

It only touches zero in the midpoint and never goes negative within the stack. Therefore, in contrast to the homogeneous state in modulated junction, *the alternating-kink state is stable with respect to short-scale perturbations*.

C. Test of short-scale instability in modulated stack with numerical simulations

We verified the short-scale instability in modulated junctions using numerical simulations described in Appendix. First, we probed the stability of the uniform state in the stack with linear modulation of the Josephson current, $j_J(x) = j_{J0}[1 + r(2x/L - 1)]$. We used the modulation parameter $r = 0.4$. If we start from the uniform n-independent state and solve the dynamic equations without noise than instability does not develop and we can trace the current-voltage dependence corresponding to this uniform state, see Fig. 2. However, if we add to the phases a small alternating perturbations, $(-1)^n\delta\varphi$, than we observe that the uniform state blows up and, after extended time evolution, it converges to the dynamic-kink state. The initial stage of this time evolution is illustrated in the lower part of Fig. 2. From the phase snapshots we can see that the instability develops near the edge with suppressed Josephson current, as the analytical analysis predicts. The upper right plot in Fig. 2 shows the time evolutions of the difference between phases in the sixth and fifth junctions at the left edge. We can see that this difference evolves from 0 corresponding to the uniform state to the value 2π corresponding to the kink state. This transition is accompanied by large-amplitude oscillations with the period much longer than the period of Josephson oscillations. These oscillations are a consequence of the small c-axis dissipation parameter, $\nu_c = 0.01$, which we used in our calculations.

We also verified that the uniform state remains stable in the stack with steplike modulation of the Josephson current, $j_J(x) = j_{J0}$ for $x > L_x/2$ and $j_J(x) = 0$ for $x < L_x/2$. The current-voltage dependence for this state is also shown in Fig. 2.

D. Homogeneous state in magnetic field

Due to the complex coupling function in the case of finite magnetic field, the short-range stability has features which are special for this case. In the regime $\ell\tilde{q} \gg 1$ the coupling to

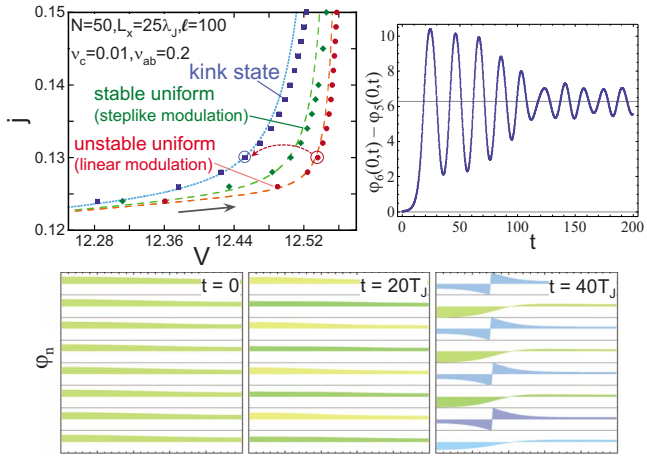

FIG. 2. (Color online) Upper left plot shows current-voltage dependences near the resonance for three dynamic states: (i) unstable uniform state in the stack with linear modulation of the Josephson current, $j_J(x)=j_{J0}[1+r(2x/L-1)]$ with $r=0.4$, (ii) kink state, and (iii) stable uniform state in the stack with steplike modulation of the Josephson current, $j_J(x)=j_{J0}\Theta(2x/L-1)$. Dashed lines show corresponding theoretical curves. Instability for the first state was triggered at the point $j=0.13$ marked at the plot. Lower plots shows snapshots of the phase distributions in the eight bottom junctions for $t=0$, $20T_J$, and $40T_J$, where $T_J=2\pi/\omega_J\approx 0.5$ is the period of Josephson oscillations for the uniform state. All phases are shifted to the range $(-\pi,\pi)$. The snapshots illustrate development of instability near the left edge. Upper right plot shows the time evolutions of the difference between phases in the sixth and fifth junctions at the left edge. This difference changes from 0 corresponding to the uniform state to 2π corresponding to the kink state.

the fast phase can be neglected, as for the modulated stack case. This means that the slow part again obeys Eq. (17) in which the local spring constant $U(x)$ now is simply given by the average cosine, $U(x)=\bar{C}(x)$. For the fundamental mode, we obtain

$$U(x) = U_\omega\left\{-\frac{\nu\omega}{\omega_1^2-\omega^2}\cos\left[h_e\left(x-\frac{L_x}{2}\right)\right] - \sin\left[h_e\left(x-\frac{L_x}{2}\right)\right]\right\}\cos\left(\frac{\pi x}{L_x}\right), \tag{21}$$

with

$$U_\omega = \frac{2h_eL_x\cos[h_eL_x/2]}{\pi^2-(h_eL_x)^2}\frac{\omega_1^2-\omega^2}{(\omega^2-\omega_1^2)^2+\nu^2\omega^2}.$$

For simplicity, we omit here the factor $(1+\alpha_r)$ in front of ω^2 which has very little influence on the short-wavelength stability. Shapes of this function at different fields is illustrated in the upper right plot of Fig. 1 for $\nu\omega/(\omega_1^2-\omega^2)=0.3$. Note that $U(x)$ always changes sign at the center, $x=L_x/2$, see, e.g., lower left plot in Fig. 1. However, for $\nu\omega\ll(\omega_1^2-\omega^2)$ the region of negative $U(x)$ is very narrow and its existence does not automatically imply instability. We analyze the central region as the most prone to instability. For $(\omega_1^2-\omega^2)\gg\nu\omega$ the spring constant behaves near $x=L_x/2$ as $U(x)\approx U_\omega[\nu\omega/(\omega_1^2-\omega^2)+h_e\tilde{x}]\pi\tilde{x}/L_x$ with $\tilde{x}=x-L_x/2$, and Eq. (17) becomes

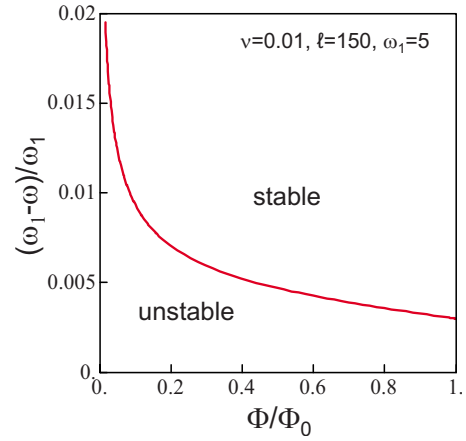

FIG. 3. (Color online) Stability range of the homogeneous state in magnetic field with respect to the short-scale phase deformations based on Eq. (22) with the listed representative parameters.

$$\left[\tilde{\Omega}^2 - U_\omega\left(\frac{\nu\omega}{\omega_1^2-\omega^2}+h_e\tilde{x}\right)\frac{\pi\tilde{x}}{L_x}\right]\tilde{\vartheta}_{\mathbf{k},0} + G_q^{-2}\frac{\partial^2\tilde{\vartheta}_{\mathbf{k},0}}{\partial\tilde{x}^2} = 0.$$

From this linear-oscillator-type equation, we derive equation for the complex eigenfrequency

$$\Omega^2/(1+\alpha\tilde{q}^2) + i\nu_c\Omega = U_\omega\left[-\frac{\nu^2\omega^2\pi/L_x}{4h_e(\omega_1^2-\omega^2)^2} + \sqrt{\frac{\pi h_e/L_x}{G_q^2U_\omega}}\right],$$

which gives the stability criterion

$$\sqrt{\frac{\pi h_e/L_x}{2\ell^2(1-\cos q)U_\omega}} > \frac{\nu^2\omega^2\pi/L_x}{4h_e(\omega_1^2-\omega^2)^2}.$$

For the most "dangerous" mode at $q=\pi$, assuming $\omega_1^2-\omega^2 \gg \nu\omega$, we obtain the following stability criterion:

$$\omega_1^2-\omega^2 > \left[\frac{\pi|g_{h,1}|\ell^2\nu^4\omega^4}{8h_e^3L_x}\right]^{1/5}. \tag{22}$$

Large value of ℓ^2 in the right-hand side is compensated by small value of $\nu^4\omega^4$. Note that increasing dissipation reduces the stability range. Taking typical values $h_e\approx 5$, $\omega_1\approx 5$, $h_eL=\pi$, $\ell=150$, and $\nu=0.002$, this inequality gives $(\omega_1-\omega)/\omega_1>1.3\times 10^{-3}$ and for larger dissipation, $\nu=0.01$, $(\omega_1-\omega)/\omega_1>0.005$. This conditions are not too restrictive. A representative stability region in the magnetic field is illustrated in Fig. 3. We conclude that the homogeneous state in the magnetic field corresponding to half-flux quantum per junction remains stable with respect to the short-scale deformations if the frequency is not too close to the resonance.

V. LONG-WAVELENGTH STABILITY

We analyze now the acoustic-type instability at very small k_y and q. With very minor modifications, this analysis applies to all dynamic states considered in this paper. Obviously, it is most relevant for the systems which are stable with respect to the short-length deformations. Consider Eq. (14) for the fast components $\tilde{\vartheta}_{\mathbf{k},\pm 1}$. At small k_y and q this equation gives the

resonance solution. To obtain approximate solution for $\tilde{\vartheta}_{\mathbf{k},\pm 1}$, we will keep only the resonance term, $\tilde{\vartheta}_{\mathbf{k},\beta}(x) \approx \psi_{\mathbf{k},\beta}\cos(m\pi x/L_x)$. Further analysis shows that the coordinate dependence of $\tilde{\vartheta}_{\mathbf{k},0}$ is weak and can be neglected. In this case, the mode amplitude $\psi_{\mathbf{k},\beta}$ can be found following the same reasoning as for the homogeneous solution leading to

$$\psi_{\mathbf{k},\beta} \approx \frac{g_m \tilde{\vartheta}_{\mathbf{k},0}/2}{\tilde{\Omega}_\beta^2 - G_{q,\beta}^{-2}(\omega_m^2 + k_y^2)}.$$

Using this result, we present Eq. (13) for the slow component $\tilde{\vartheta}_{\mathbf{k},0}$ as

$$[\tilde{\Omega}_0^2 - g(x)\bar{C}(x) - G_{q,0}^{-2}k_y^2]\tilde{\vartheta}_{\mathbf{k},0} + G_{q,0}^{-2}\frac{\partial^2 \tilde{\vartheta}_{\mathbf{k},0}}{\partial x^2} = \frac{g(x)}{4}\sum_{\beta=\pm 1}\frac{g_m \tilde{\vartheta}_{\mathbf{k},0}\cos(m\pi x/L_x)}{\tilde{\Omega}_\beta^2 - G_{q,\beta}^{-2}(\omega_m^2 + k_y^2)}. \tag{23}$$

The typical length scale for its variation, $l_\Omega = (\sqrt{|\tilde{\Omega}_0^2 - G_{q,0}^{-2}k_y^2||G_{q,0}|})^{-1}$ exceeds the stack width L_x because we consider the case of small k_y, q, and Ω when $G_{q,0} \sim 1$ and $\Omega, k_y \ll 1/L_x$. This allows us to neglect x dependence of $\tilde{\vartheta}_{\mathbf{k},0}$. In this case $g(x)\bar{C}(x)$ and $g(x)\cos(m\pi x/L_x)$ can be replaced by their averages over x

$$\langle g(x)\bar{C}(x)\rangle_x \approx -\frac{g_m^2[(1+\alpha_r)\omega^2 - \omega_m^2]/4}{[(1+\alpha_r)\omega^2 - \omega_m^2]^2 + (\nu_c + \nu_r)^2\omega^2},$$

$$\langle g(x)\cos(m\pi x/L_x)\rangle_x = g_m/2.$$

We also can neglect the charging effects because at the typical wave vector $q \sim \pi/N$ and $\alpha \lesssim 0.1$ the charging correction αq^2 is tiny and has only minor influence on stability criteria. In these approximations, the equation for $\Omega(q)$ becomes

$$\Omega^2 - \frac{k_y^2}{1 + k_z^2/[1 - i\Omega\nu_{ab}]} + i\nu_c\Omega = \frac{g_m^2}{8\omega_m}\mathcal{G}(\Omega,\mathbf{k}) \tag{24}$$

with $k_z = 2\ell\sin(q/2) \approx \ell q$, $\mathbf{k} = (k_y, k_z)$ and

$$\mathcal{G}(\Omega,\mathbf{k}) = -\frac{2\omega_m[(1+\alpha_r)\omega^2 - \omega_m^2]}{[(1+\alpha_r)\omega^2 - \omega_m^2]^2 + \nu^2\omega^2} + \sum_{\beta=\pm 1}\omega_m\left[(\Omega - \beta\omega)^2 - \frac{\omega_m^2 + k_y^2}{1 + \dfrac{k_z^2}{1 - i\nu_{ab}(\Omega - \beta\omega)}} + i\nu_c(\Omega - \beta\omega)\right]^{-1}.$$

If we eliminate the radiaton corrections, ν_r and α_r, which only appear at very small k_y and k_z then this function satisfies the translational invariance condition $\mathcal{G}(0,0)=0$. Note that we cannot take true limit $k_y, k_z \to 0$ because we consider a finite-size stack with geometrical sizes smaller than the wavelength of outside radiation.

As the Josephson frequency ω is close to the cavity-mode frequency ω_m, we can keep only the dominating resonance terms. To simplify presentation of the second term, we introduce the shift of the plasma frequency at finite k_y and k_z with respect to the homogeneous mode, $\Delta_{\mathbf{k}} = \omega_p(k_m,0,0) - \omega_p(k_m,k_y,k_z)$, and mode damping parameter, $\nu_{\mathbf{k}}$,

$$\Delta_{\mathbf{k}} + i\frac{\nu_{\mathbf{k}}}{2} = \frac{1}{2\omega_m}\left\{\omega_m^2 - \frac{\omega_m^2 + k_y^2}{1 + k_z^2/[1 - i\nu_{ab}(\Omega - \beta\omega)]}\right\} \approx \frac{\omega_m}{2}\left(\frac{k_z^2}{1 + \nu_{ab}^2\omega_m^2} - \frac{k_y^2}{k_m^2}\right) + i\frac{\omega_m^2}{2}\frac{\nu_{ab}k_z^2}{1 + \nu_{ab}^2\omega_m^2}.$$

Introducing also the resonance detuning $\delta_\omega = \omega - \omega_m$, we simplify $\mathcal{G}(\Omega,\mathbf{k})$ as

$$\mathcal{G}(\Omega,\mathbf{k}) \approx -\frac{\delta_\omega + \delta_r}{(\delta_\omega + \delta_r)^2 + \nu^2/4} + \frac{\delta_\omega + \Delta_{\mathbf{k}}}{(\delta_\omega + \Delta_{\mathbf{k}})^2 - (\Omega + i\nu_k/2)^2} \tag{25}$$

with $\delta_r = \alpha_r\omega_m/2$ being the radiation shift of the resonance frequency and

$$\nu_k \approx \nu_c + \frac{\omega_m^2\nu_{ab}k_z^2}{1 + \nu_{ab}^2\omega_m^2} \tag{26}$$

is the damping of the plasma mode at finite wave vector (we neglect small terms on the order of $k_z^2k_y^2$).

Due to the resonance structure of $\mathcal{G}(\Omega,\mathbf{k})$, in the limit $\Delta_{\mathbf{k}}, |\delta_\omega| \ll g_m/\sqrt{8\omega_m}$ it typically exceeds the right-hand side of Eq. (24) and the dispersion equation is approximately given by $\mathcal{G}(\Omega,\mathbf{k})=0$. In this approximation we obtain the following result for the eigenfrequencies:

$$\Omega_\pm(\mathbf{k}) \approx -i\frac{\nu_k}{2} \pm \sqrt{(\tilde{\delta}_\omega + \tilde{\Delta}_{\mathbf{k}})\left(\tilde{\Delta}_{\mathbf{k}} - \frac{\nu^2}{4\tilde{\delta}_\omega}\right)}, \tag{27}$$

where we introduced new notations $\tilde{\delta}_\omega = \delta_\omega + \delta_r$ and $\tilde{\Delta}_{\mathbf{k}} = \Delta_{\mathbf{k}} - \delta_r$ to absorb the radiation frequency shift. Only the mode $\Omega_+(\mathbf{k})$ is potentially unstable. The instability takes place when the expression under the square root is negative and the imaginary square root exceeds the first term. This leads to the following condition for the instability in the (k_y, k_z) plane:

$$(\tilde{\delta}_\omega + \tilde{\Delta}_{\mathbf{k}})\left(\frac{\nu^2}{4\tilde{\delta}_\omega} - \tilde{\Delta}_{\mathbf{k}}\right) > \frac{\nu_k^2}{4}. \tag{28}$$

Analysis of this criterion shows that the long-range stability is determined by several factors including behavior of the

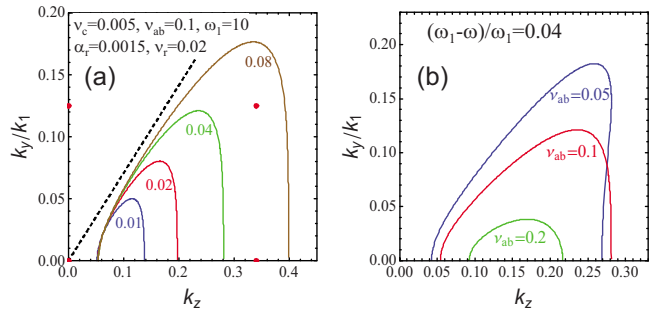

FIG. 4. (Color online) (a) Evolution of the instability region for the long-wave deformations in the k_z-k_y plane with approaching the resonance from below. Unstable regions are inside the domes. Used representative parameters are shown in the plot. The curves are marked by the value $(\tilde{\omega}_1-\omega)/\omega_1=-\tilde{\delta}_\omega/\omega_m$. Dashed line shows dependence $k_y/k_1=k_z/\sqrt{1+\nu_{ab}^2\omega_1^2}$ corresponding to condition $\omega_p(k_1,k_y,k_z)=\omega_p(k_1,0,0)$. The points illustrate discrete wave vectors for a finite-size stack. In this example, the system becomes unstable for $(\tilde{\omega}_m-\omega)/\omega_m$ between 0.04 and 0.08. (b) Evolution of the instability region in the k_z-k_y plane at fixed frequency with increasing the in-plane dissipation parameter ν_{ab}.

plasmon frequency shift $\Delta_{\mathbf{k}}$ and the relation between the damping of the homogeneous mode ν and damping of excited modes at finite wave vectors, ν_k. As the shift $\tilde{\Delta}_{\mathbf{k}}$ may take both positive and negative values depending on k_y and k_z, it is more transparent to find the instability range for this parameter,

$$\left|\tilde{\Delta}_{\mathbf{k}}+\frac{\tilde{\delta}_\omega}{2}-\frac{\nu^2}{8\tilde{\delta}_\omega}\right|<\frac{1}{2}\sqrt{\left(\tilde{\delta}_\omega+\frac{\nu^2}{4\tilde{\delta}_\omega}\right)^2-\nu_k^2}. \tag{29}$$

In particular, there is no instability in the k_z region satisfying the condition

$$\nu_k>|\tilde{\delta}_\omega|+\frac{\nu^2}{4|\tilde{\delta}_\omega|}$$

which explicitly can be written as condition for k_z

$$k_z>k_{z,i},$$

$$k_{z,i}^2=\frac{1+\nu_{ab}^2\omega_m^2}{\nu_{ab}\omega_m^2}\left[|\tilde{\delta}_\omega|+\frac{(\nu_c+\nu_r)^2}{4|\tilde{\delta}_\omega|}-\nu_c\right]. \tag{30}$$

Qualitatively, we can conclude that the in-plane dissipation suppresses instability until $\nu_{ab}\omega_m<1$ while the radiation damping enhances the instability. As for a finite-size stack the k_z values are limited from below, $k_z>\ell\pi/N$, the above equation also determines the stable frequency range for a stack with given size. We can see that this range expands with decreasing N.

In small-k_z range where the condition in Eq. (30) is not satisfied there may be a range of k_y where the system is unstable. We can find from Eq. (29) an explicit presentation for this range

$$\left|\frac{k_y^2}{k_m^2}-\frac{k_z^2}{1+\nu_{ab}^2\omega_m^2}+\frac{\tilde{\delta}_\omega}{\omega_m}-\frac{\nu^2}{4\tilde{\delta}_\omega\omega_m}\right|<\sqrt{\left(\frac{\tilde{\delta}_\omega}{\omega_m}+\frac{\nu^2}{4\tilde{\delta}_\omega\omega_m}\right)^2+\frac{\nu_k^2}{\omega_m^2}}. \tag{31}$$

The instability regions in the (k_y,k_z) plane for the different Josephson frequencies near the resonance are illustrated in Fig. 4(a). One can see that the instability region rapidly shrinks with approaching the resonance. Vanishing of instability at large k_z is caused by increasing mode damping due to the in-plane dissipation. This is illustrated in Fig. 4(b) where we plot the instability region at fixed Josephson frequency for different in-plane dissipation parameter ν_{ab}. We can see that the instability regions shrinks with increasing ν_{ab}. Existence of the instability region in the (k_y,k_z) plane does not automatically imply instability in real junction stacks. In a finite-size stack a discrete set of the wave vectors is allowed, $k_{y,m}=m\pi/L_y$, $k_{z,n}=n\ell\pi/N$. The system is only unstable if at least one of discrete pairs $(k_{y,m},k_{z,n})$ falls inside the instability region at given frequency, as illustrated in Fig. 4(a).

At finite radiation corrections and at sufficiently strong in-plane dissipation the instability region may vanish completely in some frequency range. The condition for absence of instability can be written as

$$\max_{k_z}\left[\frac{k_z^2}{1+\nu_{ab}^2\omega_m^2}-\frac{\tilde{\delta}_\omega}{\omega_m}+\frac{\nu^2}{4\tilde{\delta}_\omega\omega_m}+\sqrt{\left(\frac{\tilde{\delta}_\omega}{\omega_m}+\frac{\nu^2}{4\tilde{\delta}_\omega\omega_m}\right)^2+\frac{\nu_k^2}{\omega_m^2}}\right]<0.$$

Finding the maximum leads to the following range of frequency at which there is no instability at all

$$\left|\frac{|\delta_\omega|}{\omega_m}-\frac{W_{ab}}{2}\left(\frac{\nu_c}{\omega_m}+\omega_m\nu_{ab}\alpha_r\right)\right|<\frac{W_{ab}}{2}\sqrt{\left(\frac{\nu_c}{\omega_m}+\omega_m\nu_{ab}\alpha_r\right)^2-\frac{\nu^2}{\omega_m^2}} \tag{32}$$

with $W_{ab}=\sqrt{1+\omega_m^2\nu_{ab}^2}+\omega_m\nu_{ab}$. This region only exists if inequality $\omega_m^2\nu_{ab}\alpha_r>\nu_r$ is satisfied, leading to the following condition for the in-plane dissipation $\omega_m\nu_{ab}>2\pi/\ln[C/k_\omega L_z]$.

The largest value of k_z at which the instability boundary crosses $k_y=0$, k_{z0}, can be found as

$$k_{z0}^2=\alpha_r-\frac{\tilde{\delta}_\omega}{\omega_m}-\frac{\nu^2}{4\tilde{\delta}_\omega\omega_m}+\nu_c\nu_{ab}+\sqrt{[1+(\omega_m\nu_{ab})^2]\left(\frac{\tilde{\delta}_\omega}{\omega_m}+\frac{\nu^2}{4\tilde{\delta}_\omega\omega_m}\right)^2-\left[\frac{\nu_c}{\omega_m}+\omega_m\nu_{ab}\left(\alpha_r-\frac{\tilde{\delta}_\omega}{\omega_m}+\frac{\nu^2}{4\tilde{\delta}_\omega\omega_m}\right)\right]^2}. \tag{33}$$

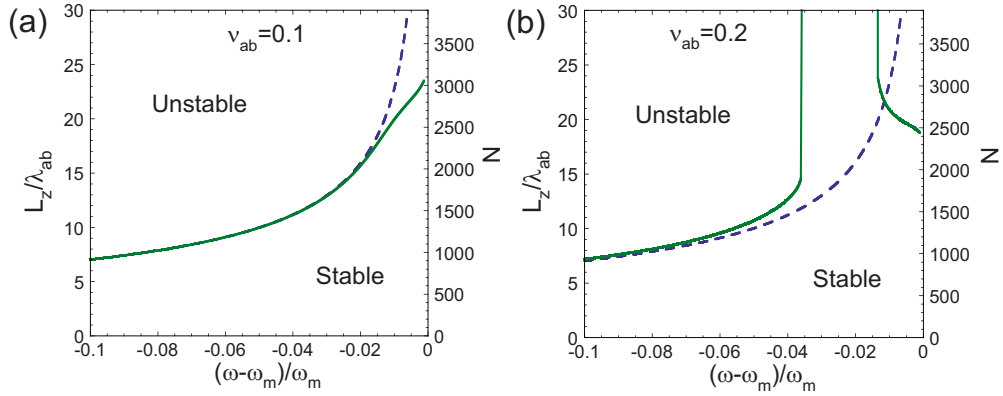

FIG. 5. (Color online) Stability range with respect to the long-wave deformations near the resonance as a function of the stack height based on Eq. (33). Two regimes are illustrated in plots (a) and (b), which are controlled by the in-plane dissipation. Dashed lines show stability boundaries without radiation corrections. In the calculations we used the following representative parameters, $\nu_c=0.005$, $\omega_1=10$, and $\ell=130$. For radiation parameters we used $\alpha_r=3.3\cdot 10^{-4}L_z/\lambda_{ab}$ and $\nu_r/\omega_1=5.2\cdot 10^{-4}L_z/\lambda_{ab}$, where the numerical coefficients were estimated assuming $\lambda_{ab}=0.25$ μm, $L_x=80$ μm, $\epsilon_c=12$, and $\ln(C/k_\omega L_z)=4$.

A finite-height stack is stable with respect to the long-range deformations if the minimum wave vector $k_{z,\min}=\pi\ell/N=\pi\lambda_{ab}/L_z$ exceeds the maximum between the two frequency-dependent wave vectors $k_{z,i}$ and k_{z0} defined by Eqs. (30) and (33) leading to the following criterion:

$$N<\frac{\pi\ell}{\max(k_{z,i},k_{z0})}. \tag{34}$$

This condition gives to the frequency-height stability diagrams illustrated in Fig. 5. As the radiation corrections α_r and ν_r are proportional to the stack height, these boundaries have to be computed self-consistently. A simple estimate for the wave vector k_{z0} can be obtained for weak in-plane dissipation $\omega_m\nu_{ab}\ll 1$ away from the resonance at $\tilde{\delta}_\omega<0$, $|\tilde{\delta}_\omega|\gg\nu,\omega_m\alpha_r$. In this case $k_{z0}^2\approx 2|\tilde{\delta}_\omega|$ meaning that the finite-height stack becomes unstable at $|\tilde{\delta}_\omega|/\omega_m>(\pi\ell/N)^2/2$.

In presence of radiation corrections, two regimes exists depending on strength of the in-plane dissipation. At small $\omega_m\nu_{ab}$ there is always the critical stack height above which the system becomes unstable. Coupling to the radiation decreases this critical height, i.e., it enhances the instability. This is in contrast to the small-size stacks away from resonances,[7] where the coupling with outside radiation stabilizes the synchronized state. This behavior changes at large in-plane dissipation. In this case a range of frequencies exists within which the system remains stable for all stack heights. Also, in this regime coupling to radiation somewhat increases the critical stack height away from the resonance.

Test of the long-range instabilities with numerical simulations

We made several approximations in our analytical derivations, which allowed us to obtain relatively simple criteria for the long-range stability. To verify validity of these approximations, we checked some of the analytical results numerically. As suggested by the representative phase diagrams shown in Fig. 5, the long-range instabilities are only expected in rather tall stacks with heights N exceeding 1000 junctions. It is very difficult to simulate such tall stacks directly. Fortunately, if we only interested in the long-range instabilities, this is not necessary. For this purpose, we simulated a coarse-grained model with the step in c-direction δz containing many junctions. As demonstrated in the Appendix, by change in variables, this coarse-grained model can be reduced to the original model with reduced parameter ℓ, $\ell\to\ell_{cg}=\ell/\delta z$. This trick allows us to use the same code with different parameters to probe the long-range stability of very tall stacks. In this case, the number of layers in the model N is replaced by the number of numerical slices $N_{cg}=N/\delta z=N\ell_{cg}/\ell$. In numerics we use the two-dimensional model which only allows us to check our analytical results in the simplest situations when the instability is homogeneous in y direction ($k_y=0$). We also neglected the layer-charging effect, $\alpha=0$, and did not take into account the radiation corrections, $\alpha_r=\nu_r=0$. Having in mind to probe the long-range stability of the kink state, we use the modulation function $g(u)=\mathrm{sgn}(u-L_x/2)$. With such modulation function the system is stable with respect to the short-scale perturbations

To probe the long-range stability, we numerically solved the dynamics equations for increasing transport current in the voltage range corresponding to the Josephson frequencies close and below the fundamental resonance. We added small deformation $\delta\varphi(u,n)\propto\cos[\pi(n-1/2)/N]$ at the beginning of every run for new value of the current and monitored the time evolution of the difference $\varphi(0,1)-\varphi(0,N_{cg})$. Figure 6 shows results of simulations of the coarse-grain model, which reveal the long-range instability. Figure 6(a) shows the current-voltage dependences near the resonance for three sets of parameters: (i) $\ell_{cg}=5$, $L_x=1.25\lambda_J\delta z$, and $N_{cg}=50$, (ii) $\ell_{cg}=10$, $L_x=2.5\lambda_J\delta z$, and $N_{cg}=50$, and (iii) $\ell_{cg}=5$, $L_x=1.25\lambda_J\delta z$, and $N_{cg}=40$. In all cases we used the dissipation parameters $\nu_c=0.01$ and $\nu_{ab}=0.2$. The values of the total stack heights $N=N_{cg}\ell/\ell_{cg}$ listed in the legend were obtained assuming $\ell=150$. For all three cases we observe the long-range instability which leads to appearance of a small additional bump in the current-voltage dependence. Development of the instability is illustrated in Fig. 6(b) in which we show time evolution of $\varphi(0,1)-\varphi(0,N_{cg})$ for different currents for

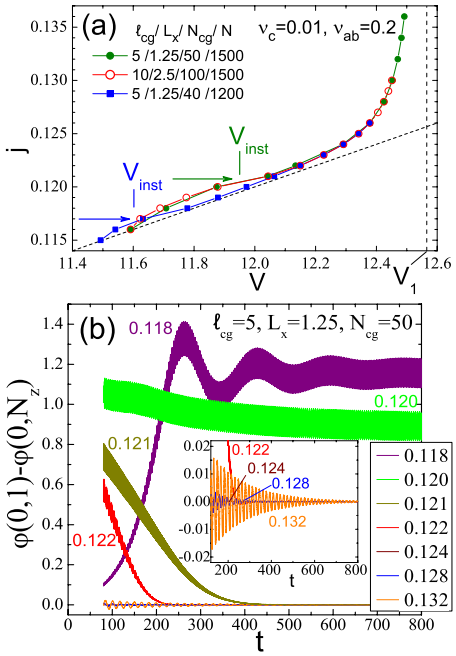

FIG. 6. (Color online) Probing the long-range instability using numerical simulations of the coarse-grained model. (a) The current-voltage dependences for three sets of parameters below the resonance voltage $V_1=4\pi$. The horizontal arrows mark onsets of instabilities in simulations and the vertical bars mark the theoretical estimates described in the text. The instability leads to appearance of a small additional bump in the current-voltage dependence. (b) The time evolution of the difference between the bottom and top phases at the left edge. One can see that for $j\geq 0.121$ this difference decays with time indicating stability of the homogeneous state while for $j\leq 0.120$ this difference remains finite. The inset shows the blowup plot of the long-time decay of the phase differences for stable states. The stripelike appearance of the curves is due to the rapid oscillations with the Josephson frequency.

the first set of parameters. We can see that for for $j\geq 0.121$ the initial perturbation decays with time indicating stability of the homogeneous state while for $j\leq 0.120$ the perturbation does not decay. The instability onsets are marked by the horizontal arrows in Fig. 6(a). The sets of parameters (i) and (ii) correspond to simulations of the same physical system with two different coarse-graining parameters, $\delta z=30$ and 15 (assuming $\ell=150$). We observed that in both cases the instability develops at the same voltage indicating that the coarse graining does not influence much the long-range stability. The set (iii) has the same parameters as the set (i), except for the smaller height. We see that the instability moved to the lower voltage, as expected.

We now compare the location of the instability onset with the analytical predictions. At $k_y=0$ the condition of stability is given by $\pi\ell/N>k_{z0}$ and, without the radiation corrections, formula (33) for k_{z0} significantly simplifies

$$k_{z0}^2=2\left(\frac{|\delta_\omega|}{\omega_1}-\frac{\nu_c^2}{4|\delta_\omega|\omega_1}-\nu_c\nu_{ab}\right),\quad \text{for}\ \ \alpha_r,\nu_r=0. \quad (35)$$

Moreover, for the parameters we used in simulations the terms with ν_c are negligible and with high accuracy we can estimate the shift from the resonance where the instability is expected as

$$|\delta_\omega|\approx(\omega_1/2)(\pi\ell/N)^2=(\omega_1/2)(\pi\ell_{\rm cg}/N_{\rm cg})^2.$$

This gives $|\delta_\omega|\approx 0.62$, $V_{\rm inst}=\omega_1-|\delta_\omega|\approx 11.95$ for the first and second sets of parameters and $|\delta_\omega|\approx 0.97$, $V_{\rm inst}\approx 11.6$ for the third set. These values are shown by the vertical bars in Fig. 6(a). We see that in the simulations the instabilities appear *exactly* where they are predicted analytically. This gives us a confidence that the used approximations are legitimate.

With simulations we can go beyond finding the location of the instability onset. We can also find the finite dynamic state after the instability develops. To understand the structure of this finite state, we present in Fig. 7 snapshots of the distribution of the electric field for the first set of parameters at $j=0.12$. Analyzing these snapshots, we conclude that the instability leads to the state in which the oscillating phase is a superposition of two modes,

$$\theta_{\omega,n}(x)=\{\Psi_{1,0}+i\Psi_{1,1}\cos[\pi(n-1/2)/N]\}\cos(\pi x/L_x),$$

where the amplitude of the nonuniform mode, $\Psi_{1,1}$, continuously grows starting from zero at the instability onset.

VI. SUMMARY

In conclusion, we found that dynamical states synchronized by the internal cavity resonance are prone to two very different instabilities. *The short-wavelength* instability develops for states which have regions of negative time-averaged Josephson coupling. In particular, the homogeneous state in stacks with modulated Josephson coupling typically has this type of instability. The homogeneous state in the external magnetic field $H<\Phi_0/(sL_x)$ has this type of instability close

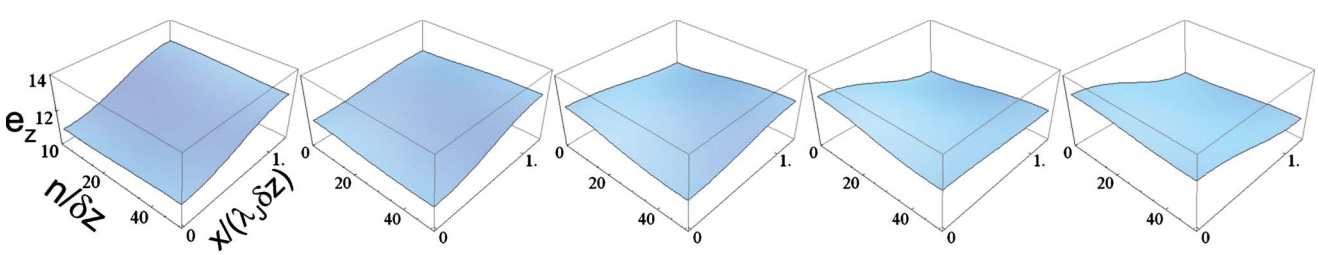

FIG. 7. (Color online) Snapshots of the distribution of the electric field for the steady state in the unstable region for the first set of parameters in the previous figure at $j=0.12$ over the half period of the Josephson oscillations. One can see the contribution from the nonuniform mode.

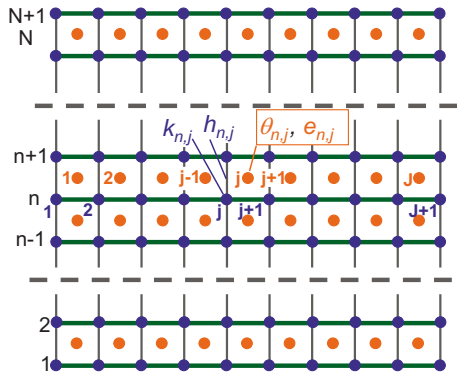

FIG. 8. (Color online) Illustration of the staggered grid used for numerical solution of the dynamic Eqs. (A1)–(A4).

to the resonance and the instability range widens with decreasing field. *The long-wavelength* instability appears due to the parametric resonance excitation of the fast modes at finite wave vectors. The instability criterion depends on the relation between the damping of the homogeneous mode and modes at finite wave vectors. Finite-height stacks are stable sufficiently close to the resonance. The instability region typically shrinks with increasing in-plane dissipation.

ACKNOWLEDGMENTS

I would like to acknowledge many useful discussions with U. Welp, L. Bulaevskii, X. Hu, S. Z. Lin, K. Gray, L. Ozyuzer, K. Kadowaki, H. Wang, and R. Kleiner. This work was supported by UChicago Argonne, LLC, operator of Argonne National Laboratory, a U.S. Department of Energy Office of Science laboratory, operated under Contract No. DE-AC02-06CH11357.

APPENDIX: NUMERICAL SIMULATIONS AND COARSE-GRAINING PROCEDURE

For numerical simulations it is convenient to present the dynamic equations in the form of the time-evolution equations for the reduced c-axis electric fields (e_n), phases (φ_n), in-plane supermomenta (k_n), and magnetic fields (h_n),

$$\frac{\partial e_n}{\partial \tau} = -\nu_c e_n - g(u)\sin\varphi_n + \frac{\partial h_n}{\partial u}, \tag{A1}$$

$$\frac{\partial \varphi_n}{\partial \tau} = e_n, \tag{A2}$$

$$\nu_{ab}\frac{\partial k_n}{\partial \tau} = -[k_n + h_n - h_{n-1}], \tag{A3}$$

$$h_n = \ell^2\left(\frac{\partial \varphi_n}{\partial u} - k_{n+1} + k_n\right). \tag{A4}$$

The units in these equations are different from units used for analytical calculations: unit of length is the Josephson length λ_J, unit of supermomentum is $1/\lambda_J$, unit of magnetic field is $\Phi_0/(2\pi\gamma\lambda^2)$, and unit of electric field is $\Phi_0\omega_p/(2\pi cs)$. All parameters are assumed to be y independent. Therefore we only probe instabilities uniform in this direction. We also neglected the layer-charging effect, $\alpha=0$. Above equations are solved for stack containing N junctions with $0<u<L_x$ assuming simple nonradiative boundary conditions at the edges, $k_n=0$, $\partial\varphi_n/\partial u = \mp I/2\ell^2$ at $u=0,L_x$, where $I=jL_x$ is the total transport current

Solution of these equations is implemented using the following implicit numerical scheme.

(1) Space and time discretizations are performed using a staggered grid. For coordinate, $\varphi_n(u,\tau)$ and $e_n(u,\tau)$ are defined at the points $u=(j-1/2)d_u$ while $k_n(u,\tau)$ and $h_n(u,\tau)$ are defined at the points $u=jd_u$, see Fig. 8. For time, e_n is defined at $\tau=md_\tau$ while φ_n, k_n, and h_n are defined at $\tau=(m+1/2)d_\tau$.

$$\varphi_{n,j}^{m+1/2} = \varphi_n[(j-1/2)d_u,(m+1/2)d_\tau],$$

$$e_{n,j}^{m} = e_n[(j-1/2)d_u,md_\tau], \quad 1<j<J,$$

$$k_{n,j}^{m+1/2} = k_n[(j-1)d_u,(m+1/2)d_\tau],$$

$$h_{n,j}^{m+1/2} = h_n[(j-1)d_u,(m+1/2)d_\tau], \quad 1<j<J+1.$$

(2) We discretize equations as

$$\frac{e_{n,j}^{m+1}-e_{n,j}^{m}}{d_\tau} = -\nu_c\frac{e_{n,j}^{m+1}+e_{n,j}^{m}}{2} - g_j\sin\varphi_{n,j}^{m+1/2} + \frac{h_{n,j+1}^{m+1/2}-h_{n,j}^{m+1/2}}{d_u}, \tag{A5}$$

$$\frac{\varphi_{n,j}^{m+3/2}-\varphi_{n,j}^{m+1/2}}{d_\tau} = e_n^{m+1}, \tag{A6}$$

$$\frac{k_{n,j}^{m+3/2}-k_{n,j}^{m+1/2}}{d_\tau} = -\frac{1}{\nu_{ab}}\left[\frac{k_{n,j}^{m+3/2}+k_{n,j}^{m+1/2}}{2} + \frac{h_{n,j}^{m+3/2}+h_{n,j}^{m+1/2}}{2} - \frac{h_{n-1,j}^{m+3/2}+h_{n-1,j}^{m+1/2}}{2}\right], \tag{A7}$$

$$h_{n,j}^{m+3/2} = \ell^2\left(\frac{\varphi_{n,j}^{m+3/2}-\varphi_{n,j-1}^{m+3/2}}{d_u} - k_{n+1,j}^{m+3/2} + k_{n,j}^{m+3/2}\right). \tag{A8}$$

(3) The first two equations allow for direct time advance of $e_{n,j}$ and $\varphi_{n,j}$

$$e_{n,j}^{m+1} = \left(\frac{1}{d_\tau}+\frac{\nu_c}{2}\right)^{-1}\left[\left(\frac{1}{d_\tau}-\frac{\nu_c}{2}\right)e_{n,j}^{m} - g_j\sin\varphi_{n,j}^{m+1/2} + \frac{h_{n,j+1}^{m+1/2}-h_{n,j}^{m+1/2}}{d_u}\right],$$

$$\varphi_{n,j}^{m+3/2} = \varphi_{n,j}^{m+1/2} + d_\tau e_n^{m+1}.$$

(4) Substitution of $h_{n,j}^{m+3/2}$ and $h_{n-1,j}^{m+3/2}$ from Eq. (A8) into Eq. (A7) leads to the tridiagonal linear system for $k_{n,j}^{m+3/2}$,

$$\ell^2 k_{n+1,j}^{m+3/2} - \left(1 + \frac{2\nu_{ab}}{d_\tau} + 2\ell^2\right) k_{n,j}^{m+3/2} + \ell^2 k_{n-1,j}^{m+3/2}$$
$$= \left(1 - \frac{2\nu_{ab}}{d_\tau}\right) k_{n,j}^{m+1/2} + \ell^2 \frac{\varphi_{n,j}^{m+3/2} - \varphi_{n,j-1}^{m+3/2} - \varphi_{n-1,j}^{m+3/2} + \varphi_{n-1,j-1}^{m+3/2}}{d_u}$$
$$+ h_{n,j}^{m+1/2} - h_{n-1,j}^{m+1/2}$$

for $n=2,\ldots,N$ with $k_{1,j}^{m+3/2}=0$; $k_{N+1,j}^{m+3/2}=0$. Solving this system, we advance $k_{n,j}$

(5) After finding $k_{n,j}^{m+3/2}$, we update $h_{n,j}^{m+3/2}$ using Eq. (A8). The long-range instabilities are only expected for very tall stacks $N>1000$ which are very difficult to simulate directly. To probe these instabilities, we use the coarse-grained model. Assuming that the perturbations are smooth in z direction we introduce a discretization step δz containing many junctions, $\delta z \gg 1$, and write coarse-grained equations only for junctions with $n=\delta z m$,

$$\frac{\partial e_m}{\partial \tau} = -\nu_c e_m - g(u)\sin\varphi_m + \frac{\partial h_m}{\partial u},$$

$$\frac{\partial \varphi_m}{\partial \tau} = e_m,$$

$$\frac{\partial k_m}{\partial \tau} = -\frac{1}{\nu_{ab}}\left[k_m + \frac{h_m - h_{m-1}}{\delta z}\right],$$

$$h_m = \ell^2\left(\frac{\partial \varphi_m}{\partial u} - \frac{k_{m+1} - k_m}{\delta z}\right).$$

Transforming variables, $u=\delta z\tilde{u}$, $h_m=\tilde{h}_m\delta z$, we arrive to original Eqs. (A1)–(A4) with replacements $u\to\tilde{u}$, $h_m\to\tilde{h}_m$, and $\ell\to\ell_{cg}=\ell/\delta z=\lambda/\delta z s$. Therefore, *simulations of the same model with the smaller parameter ℓ is equivalent to coarse graining* and allows us to explore the long-range instabilities in very tall stacks. Renormalization implies that the stack width is now measured in units $\lambda_J\delta z$. The effective stack height is given by $N=\delta z N_{cg}$, where N_{cg} is the total number of the c-axis slices in the coarse-grained model. Having in mind to probe the long-range stability of the kink state, we use the modulation function $g(u)=\mathrm{sgn}(u-L_x/2)$. With such modulation function the system is stable with respect to the short-scale perturbations

[1] B. D. Josephson, Phys. Lett. **1**, 251 (1962).
[2] A. K. Jain, K. K. Likharev, J. E. Lukens, and J. E. Sauvageau, Phys. Rep. **109**, 309 (1984).
[3] M. Darula, T. Doderer, and S. Beuven, Supercond. Sci. Technol. **12**, R1 (1999).
[4] P. Barbara, A. B. Cawthorne, S. V. Shitov, and C. J. Lobb, Phys. Rev. Lett. **82**, 1963 (1999); B. Vasilić, S. V. Shitov, C. J. Lobb, and P. Barbara, Appl. Phys. Lett. **78**, 1137 (2001); B. Vasilić, P. Barbara, S. V. Shitov, and C. J. Lobb, Phys. Rev. B **65**, 180503(R) (2002).
[5] F. Song, F. Muller, R. Behr, and A. M. Klushin, Appl. Phys. Lett. **95**, 172501 (2009).
[6] R. Kleiner, F. Steinmeyer, G. Kunkel, and P. Müller, Phys. Rev. Lett. **68**, 2394 (1992); R. Kleiner and P. Müller, Phys. Rev. B **49**, 1327 (1994).
[7] L. N. Bulaevskii and A. E. Koshelev, Phys. Rev. Lett. **99**, 057002 (2007).
[8] L. Ozyuzer, A. E. Koshelev, C. Kurter, N. Gopalsami, Q. Li, M. Tachiki, K. Kadowaki, T. Yamamoto, H. Minami, H. Yamaguchi, T. Tachiki, K. E. Gray, W.-K. Kwok, and U. Welp, Science **318**, 1291 (2007); K. E. Gray, A. E. Koshelev, C. Kurter, K. Kadowaki, T. Yamamoto, H. Minami, H. Yamaguchi, M. Tachiki, W.-K. Kwok, and U. Welp, IEEE Trans. Appl. Supercond. **19**, 886 (2009).
[9] A. E. Koshelev and L. N. Bulaevskii, Phys. Rev. B **77**, 014530 (2008).
[10] K. Kadowaki, H. Yamaguchi, K. Kawamata, T. Yamamoto, H. Minami, I. Kakeya, U. Welp, L. Ozyuzer, A. Koshelev, C. Kurter, K. E. Gray, and W.-K. Kwok, Physica C **468**, 634 (2008); H. Minami, I. Kakeya, H. Yamaguchi, T. Yamamoto, and K. Kadowaki, Appl. Phys. Lett. **95**, 232511 (2009); K. Kadowaki, M. Tsujimoto, K. Yamaki, T. Yamamoto, T. Kashiwagi, H. Minami, M. Tachiki, and R. A. Klemm, J. Phys. Soc. Jpn. **79**, 023703 (2010); M. Tsujimoto, K. Yamaki, K. Deguchi, T. Yamamoto, T. Kashiwagi, H. Minami, M. Tachiki, K. Kadowaki, and R. A. Klemm, Phys. Rev. Lett. **105**, 037005 (2010).
[11] H. B. Wang, S. Gue'non, J. Yuan, A. Iishi, S. Arisawa, T. Hatano, T. Yamashita, D. Koelle, and R. Kleiner, Phys. Rev. Lett. **102**, 017006 (2009); H. Wang, S. Gu'enon, B. Gross, J. Yuan, Z. Jiang, Y. Zhong, M. Gruenzweig, A. Iishi, P. Wu, T. Hatano, D. Koelle, and R. Kleiner, *ibid.* **105**, 069902 (2010).
[12] Sh. Lin and X. Hu, Phys. Rev. Lett. **100**, 247006 (2008); Phys. Rev. B **79**, 104507 (2009).
[13] A. E. Koshelev, Phys. Rev. B **78**, 174509 (2008).
[14] A. E. Koshelev and L. N. Bulaevskii, J. Phys.: Conf. Ser. **150**, 052124 (2009).
[15] I. Kakeya, M. Iwase, T. Yamamoto, and K. Kadowaki, arXiv:cond-mat/0503498 (unpublished); S. Urayama, T. Hatano, H. Wang, M. Nagao, S. Kim, and J. Arai, arXiv:cond-mat/0602659 (unpublished); I. Kakeya, Y. Kubo, M. Kohri, M. Iwase, T. Yamamoto, and K. Kadowaki, Phys. Rev. B **79**, 212503 (2009); A. Koshelev, *ibid.* **75**, 214513 (2007).
[16] S. N. Artemenko and S. V. Remizov, Phys. Rev. B **67**, 144516 (2003).
[17] A. L. Rakhmanov, S. E. Savel'ev, and F. Nori, Phys. Rev. B **79**, 184504 (2009).
[18] P. Hadley, M. R. Beasley, and K. Wiesenfeld, Phys. Rev. B **38**, 8712 (1988).
[19] A. A. Chernikov and G. Schmidt, Phys. Rev. E **52**, 3415 (1995).
[20] S. Sakai, P. Bodin, and N. F. Pedersen, J. Appl. Phys. **73**, 2411 (1993); L. N. Bulaevskii, D. Domínguez, M. P. Maley, A. R. Bishop, and B. I. Ivlev, Phys. Rev. B **53**, 14601 (1996); S. N. Artemenko and S. V. Remizov, JETP Lett. **66**, 853 (1997).
[21] M. Machida, T. Koyama, and M. Tachiki, Phys. Rev. Lett. **83**, 4618 (1999); R. Kleiner, T. Gaber, and G. Hechtfischer, Phys. Rev. B **62**, 4086 (2000); M. Tachiki, M. Iizuka, K. Minami, S.

Tejima, and H. Nakamura, *ibid.* **71**, 134515 (2005); S. Madsen and N. F. Pedersen, *ibid.* **72**, 134523 (2005); B. Y. Zhu, H. B. Wang, S. M. Kim, S. Urayama, T. Hatano, and X. Hu, *ibid.* **72**, 174514 (2005); S. Savel'ev, V. Yampol'skii, A. Rakhmanov, and F. Nori, *ibid.* **72**, 144515 (2005); S. Lin, Xiao Hu, and M. Tachiki, *ibid.* **77**, 014507 (2008).

[22] T. Koyama and M. Tachiki, Phys. Rev. B **54**, 16183 (1996).

[23] We neglect small correction to the phase coming from self-field of transport current. It has a negligible influence on our results.

[24] The mesas, in which resonance terahertz emission was detected in Ref. 8, were fabricated on the top of bulk crystals. In this case, the dominating dissipation channel is leaking of radiation into the base crystal (Ref. 14). Stability analysis in this case is more complicated and we are not doing it in this paper.

[25] I. O. Kulik, Pis'ma ZhETF **2**, 134 (1965) [JETP Lett. **2**, 84 (1965)].

[26] L. N. Bulaevskii and A. E. Koshelev, Phys. Rev. Lett. **97**, 267001 (2006).